# Near-field spectroscopy and tuning of sub-surface modes in plasmonic terahertz resonators

**O. Mitrofanov,[1,2,*] Y. Todorov,[3,5] D. Gacemi,[3] A. Mottaghizadeh,[3] C. Sirtori,[3] I. Brener,[2,4] and J. L. Reno[2,4]**

[1] *University College London, Torrington Place, London, WC1E 7JE, UK*
[2] *Center for Integrated Nanotechnologies, Sandia National Laboratories, Albuquerque, NM 87185, USA*
[3] *Univ. Paris Diderot, Sorbonne Paris Cité, Laboratoire Matériaux et Phénomènes Quantiques, UMR 7162, CNRS, F-75205, Paris, France*
[4] *Sandia National Laboratories, Albuquerque, NM 87185, USA*
[5] *yanko.todorov@univ-paris-diderot.fr*
* *o.mitrofanov@ucl.ac.uk*

**Abstract:** Highly confined modes in THz plasmonic resonators comprising two metallic elements can enhance light-matter interaction for efficient THz optoelectronic devices. We demonstrate that sub-surface modes in such double-metal resonators can be revealed with an aperture-type near-field probe and THz time-domain spectroscopy despite strong mode confinement in the dielectric spacer. The sub-surface modes couple a fraction of their energy to the resonator surface via surface waves, which we detected with the near-field probe. We investigated two resonator geometries: a $\lambda/2$ double-metal patch antenna with a 2 μm thick dielectric spacer, and a three-dimensional meta-atom resonator. THz time-domain spectroscopy analysis of the fields at the resonator surface displays spectral signatures of sub-surface modes. Investigations of strong light-matter coupling in resonators with sub-surface modes therefore can be assisted by the aperture-type THz near-field probes. Furthermore, near-field interaction of the probe with the resonator enables tuning of the resonance frequency for the spacer mode in the antenna geometry from 1.6 to 1.9 THz (~15%).



**OCIS codes:** (160.3918) Metamaterials; (260.3090) Infrared, far; (260.5740) Resonance; (300.6495) Spectroscopy, terahertz; (300.6500) Spectroscopy, time-resolved; (310.6628) Subwavelength structures, nanostructures.

## References and links

1. E. Rosencher, and B. Vinter, *Optoelectronics* (Cambridge University, 2002).
2. D. K. Gramotnev and S. I. Bozhevolnyi, "Plasmonics beyond the diffraction limit," Nat. Photonics **4,** 83 (2010).
3. S. A. Maier, "Plasmonic field enhancement and SERS in the effective mode volume picture," Opt. Express **14,** 1957 (2006).
4. D. Palaferri, Y. Todorov, Y. N. Chen, J. Madeo, A. Vasanelli, L. H. Li, A. G. Davies, E. H. Linfield, and C. Sirtori, "Patch antenna terahertz photodetectors," Appl. Phys. Lett. **106,** 161102 (2015).
5. B. S. Williams, "Terahertz quantum-cascade lasers," Nat. Photonics **1,** 517 (2007).
6. J. Lee, M. Tymchenko, C. Argyropoulos, P.-Y. Chen, F. Lu, F. Demmerle, G. Boehm, M.-C. Amann, A. Alù and M.A. Belkin, "Giant nonlinear response from plasmonic metasurfaces coupled to intersubband transitions," Nature **511,** 65 (2014).
7. D. Palaferri, Y. Todorov, A. Mottaghizadeh, G. Frucci, G. Biasiol, and C. Sirtori, "Ultra-subwavelength resonators for high temperature high performance quantum detectors," New J. Phys. **18,** 113016 (2016).
8. F. Alves, D. Grbovic, B. Kearney, and G. Karunasiri, "Microelectromechanical systems bimaterial terahertz sensor with integrated metamaterial absorber," Opt. Lett. **37,** 1886 (2012).
9. T. J. Cui, M. Q. Qi, X. Wan, J. Zhao and Q. Cheng, "Coding metamaterials, digital metamaterials and programmable metamaterials," Light: Science & Applications **3,** e218 (2014).
10. J. Grant, Y. Ma, S. Saha, A. Khalid, and D. R. S. Cumming, "Polarization insensitive, broadband terahertz metamaterial absorber," Opt. Lett. **36,** 3476 (2011).

11. Y. Todorov, L. Tosetto, J. Teissier, A. M. Andrews, P. Klang, R. Colombelli, I. Sagnes, G. Strasser, and C. Sirtori, "Optical properties of metal-dielectric-metal microcavities in the THz frequency range," Opt. Express **18**, 13886 (2010).
12. C. Feuillet-Palma, Y. Todorov, A. Vasanelli, and C. Sirtori, "Strong near field enhancement in THz nano-antenna arrays," Sci. Rep. **3,** 1361 (2013).
13. M. Geiser, F. Castellano, G. Scalari, M. Beck, L. Nevou, and J. Faist, "Ultrastrong coupling regime and plasmon polaritons in parabolic semiconductor quantum wells," Phys. Rev. Lett. **108,** 106402 (2012).
14. E. Strupiechonski, G. Xu, M. Brekenfeld, Y. Todorov, N. Isac, A. M. Andrews, P. Klang, C. Sirtori, G. Strasser, A. Degiron, and R. Colombelli, "Sub-diffraction-limit semiconductor resonators operating on the fundamental magnetic resonance," Appl. Phys. Lett. **100,** 131113 (2012).
15. R. Singh, C. Rockstuhl, and W. Zhang, "Strong influence of packing density in terahertz metamaterials," Appl. Phys. Lett. **97,** 241108 (2010).
16. P. Alonso-Gonzalez, M. Schnell, P. Sarriugarte, H. Sobhani, C. Wu, N. Arju, A. Khanikaev, F. Golmar, P. Albella, L. Arzubiaga, F. Casanova, L. E. Hueso, P. Nordlander, G. Shvets, and R. Hillenbrand, "Real-Space Mapping of Fano Interference in Plasmonic Metamolecules," Nano Letters 11 (9), 3922 (2011).
17. T. G. Habteyes, S. Dhuey, K. I. Kiesow, and A. Vold, "Probe-sample optical interaction: size and wavelength dependence in localized plasmon near-field imaging," Opt. Express 21, 21607 (2013).
18. Y. Todorov, P. Desfonds, C. Belacel, L. Becerra, and C. Sirtori, "Three-dimensional THz lumped-circuit resonators," Opt. Express **23,** 16838, (2015).
19. A. Mottaghizadeh, Y. Todorov, M. Cameau, D. Gacemi, A. Vasanelli, and C. Sirtori, "Nanoscale electromagnetic confinement in THz circuit resonators," Opt. Express **25**, 28718 (2017).
20. A. Bitzer, H. Merbold, A. Thoman, T. Feurer, H. Helm, and M. Walther, "Terahertz near-field imaging of electric and magnetic resonances of a planar metamaterial," Opt. Express **17,** 3826 (2009).
21. J. R. Knab, A. J. L. Adam, M. Nagel, E. Shaner, M. A. Seo, D. S. Kim, and P. C. M. Planken, "Terahertz Near-Field Vectorial Imaging of Subwavelength Apertures and Aperture Arrays," Opt. Express **17,** 15072 (2009).
22. A. Bitzer, A. Ortner, H. Merbold, T. Feurer, and M. Walther, "Terahertz near-field microscopy of complementary planar metamaterials: Babinet's principle," Opt. Express **19,** 2537 (2011).
23. R. Mueckstein, C. Graham, C. C. Renaud, A. J. Seeds, J. A. Harrington, and O. Mitrofanov, "Imaging and Analysis of THz Surface Plasmon Polariton Waves with the Integrated Sub-wavelength Aperture Probe," J. Infrared, Millimeter, Terahertz Waves **32,** 1031 (2011).
24. F. Blanchard, K. Ooi, T. Tanaka, A. Doi, and K. Tanaka, "Terahertz spectroscopy of the reactive and radiative near-field zones of split ring resonator," Opt. Express **20,** 19395 (2012).
25. I. Khromova, M. Navarro-Cía, I. Brener, J. L. Reno, A. Ponomarev, and O. Mitrofanov. "Dipolar resonances in conductive carbon micro-fibers probed by near-field terahertz spectroscopy," Appl. Phys. Lett. **107,** 021102 (2015).
26. I. Khromova, P. Kužel, I. Brener, J. L. Reno, U.-C. Chung Seu, C. Elissalde, M. Maglione, P. Mounaix, and O. Mitrofanov, "Splitting of magnetic dipole modes in anisotropic $TiO_2$ micro-spheres," Laser Photonics Rev. **10,** 681 (2016).
27. A. Bhattacharya and J. Gómez Rivas, "Full vectorial mapping of the complex electric near-fields of THz resonators," APL Photonics **1,** 8 (2016).
28. N. Kumar, A. C. Strikwerda, K. Fan, X. Zhang, R. D. Averitt, P. C. M. Planken, and A. J. L. Adam, "THz near-field Faraday imaging in hybrid metamaterials," Opt. Express **20,** 11277 (2012).
29. O. Mitrofanov, I. Khromova, T. Siday, R. Thompson, A. Ponomarev, I. Brener, and J. Reno, "Near-Field Spectroscopy and Imaging of Subwavelength Plasmonic Terahertz Resonators," IEEE Trans. Terahertz Sci. Technol. **6,** 382 (2016).
30. O. Mitrofanov, Z. Han, F. Ding, S. I. Bozhevolnyi, I. Brener, and J. L. Reno, "Detection of internal fields in double-metal terahertz resonators," Appl. Phys. Lett. **110,** 061109 (2017).
31. E. Verhagen, J. A. Dionne, L. Kuipers, H. A. Atwater, and A. Polman, "Near-Field Visualization of Strongly Confined Surface Plasmon Polaritons in Metal−Insulator−Metal Waveguides," Nano Letters **8**(9), 2925 (2008).
32. J. F. Zhou, T. Koschny, and C. M. Soukoulis, "Magnetic and electric excitations in split-ring resonators," Opt. Express **15,** 17881 (2007).
33. C. A. Balanis, *Antenna Theory* (New York: John Wiley & Sons, 2005).
34. C. Feuillet-Palma, Y. Todorov, R. Steed, A. Vasanelli, G. Biasiol, L. Sorba, and C. Sirtori, "Extremely sub-wavelength THz metal-dielectric wire microcavities" Opt. Express **20**, 29121 (2012).
35. A. J. Macfaden, J. L. Reno, I. Brener, and O. Mitrofanov, "3 μm aperture probes for near-field terahertz transmission microscopy," Appl. Phys. Lett. **104,** 011110 (2014).
36. M. Natrella, O. Mitrofanov, R. Mueckstein, C. Graham, C. C. Renaud, and A. J. Seeds, "Modelling of surface waves on a THz antenna detected by a near-field probe," Opt. Express **20,** 16023-16031 (2012).
37. O. Mitrofanov, L. N. Pfeiffer, and K. W. West, "Generation of low-frequency components due to phase-amplitude modulation of subcycle far-infrared pulses in near-field diffraction," Appl. Phys. Lett. **81,** 1579 (2002).
38. S. Nagai, T. Hayashi and A. Sanada, "Measurements of anomalous skin effect in 1 THz band," IEEE MTT-S International Microwave Symposium Digest (MTT), Seattle, WA, 2013, pp. 1-3.
39. D. Denkova, N. Verellen, A. V. Silhanek, V. K. Valev, P. Van Dorpe, and V. V. Moshchalkov, "Mapping Magnetic Near-Field Distributions of Plasmonic Nanoantennas," ACS Nano **7**(4), 3168 (2013).

40. D. K. Singh, J. Sung Ahn, S. Koo, T. Kang, J. Kim, S. Lee, N. Park, and D.-S. Kim, "Selective electric and magnetic sensitivity of aperture probes," Opt. Express **23,** 20820 (2015).
41. A. Christ, H. Yekinci, H. Solak, N. A. Gippius, S. G. Tikhodeev and O. J. F. Martin, "Controlling the Fano interference in a plasmonic lattice," Phys. Rev. B **76,** 201405 (2007).
42. F. Neubrech, A. Pucci, T. W. Cornelius, S. Karim, A. Gracia-Etxarri and J. Aizpurua, "Resonant plasmonic and vibrational coupling in a tailored nanoantenna for infrared detection," Phys. Rev. Lett. **101,** 157403 (2008).
43. B. Luk'yanchuk, N. L. Zheludev, S. A. Maier, N. J. Halas, P. Nordlander, H. Giessen and C. T. Chong, "The Fano resonance in plasmonic nanostructures and metamaterials," Nat. Mat. **9,** 707-715 (2010).
44. Y. Todorov, A. M. Andrews, R. Colombelli, S. De Liberato, C. Ciuti, P. Klang, G. Strasser, and C. Sirtori, "Ultrastrong Light-Matter Coupling Regime with Polariton Dots," Phys. Rev. Lett. **105**(19), 196402 (2010).

## 1. Introduction

Optoelectronic devices rely on efficient coupling between light and electronic systems, such as semiconductors quantum wells or quantum dots [1]. In the terahertz (THz) spectral range it is essential to engineer and enhance this coupling, because the wavelength $\lambda$ (~100 μm) is more than three orders of magnitude larger than the typical size of semiconductor systems (<100 nm). The *double-metal* design, consisting of two metallic elements separated by a semiconductor spacer that is also referred to as the *metal-insulator-metal* resonator [2], enables confinement of THz fields to deeply subwavelength volumes, less than $10^{-4}\ \lambda^3$ [3], whereas the resonator geometry enhances the coupling of free-space propagating waves in a selected frequency range. THz double-metal resonators therefore have been at the forefront of research on efficient THz detectors [4], quantum cascade lasers [5], as well as for non-linear optics applications [6]. In addition to the optoelectronic applications, double-metal resonators are attractive as building blocks for metasurfaces due to their subwavelength dimensions [7]. THz double-metal resonator arrays were also employed as bolometric absorbers [8], phase control/phase shaping devices [9] and perfect absorbers [10].

Spectroscopic analysis of THz double-metal resonators however is a challenging experimental problem. A double-metal resonator often has a small scattering cross-section due to its sub-wavelength size [7]. To enhance the spectroscopic signature, double-metal resonators are studied by probing reflectivity or transmission spectra in arrays, which combine the contribution of individual resonators [11-14]. Dense arrays indeed enhance the contrast in spectral features [7,12,15], however the collective response is more complex in comparison to that of a single resonator [15]. Furthermore, double-metal resonators can support high-symmetry modes, which are generally non-radiative (dark), and thus become invisible for far-field spectroscopy [11]. Near-field microscopy techniques on the other hand can reveal dark modes [16,17]. Another challenge in far-field experiments, especially for resonator architectures without a full metallic ground plane, is the presence of a thick substrate, which introduces substrate modes seen as Fabry-Perot oscillations in the measured spectra, and further increases the interaction between individual resonators. These limitations become particularly severe for resonator designs, which confine THz fields to the nanoscale dimensions [18,19].

THz near-field spectroscopy and microscopy methods enabled experimental characterization of planar THz plasmonic resonators in arrays [20-22] and as single elements [23-27] by sensing evanescent electromagnetic fields near the surface. The near-field approach can reveal resonator modes, with their spectra [24-29], and the electric and magnetic field distributions on the surface [27,28], as well as temporal evolution of the resonance excitation [23,29]. The double-metal design however presents a challenge for experimental probing [30,31]: the electromagnetic energy of the spacer mode is confined between two closely-spaced metallic elements, below the resonator surface. As a result, THz near-field spectroscopy and mapping of the subsurface modes in double-metal resonators have so far remained outside the reach of the near-field techniques, with exception of a recently proposed special method, which exploited the effect of image charges [30].

Here we show that despite the strong field confinement within the resonator, aperture-type THz near-field microscopy and THz time-domain spectroscopy can nevertheless probe

sub-surface modes in double-metal resonators of different geometries. We chose the collection-mode aperture-type THz near-field probe in this study because it enables the same normal incidence excitation of the resonator, as realized in practical applications of metasurfaces and resonator arrays. In contrast, the scattering type THz near-field microscopy method typically requires the excitation wave to be incident at an angle of 45-60°. Furthermore the scattering probe tip must be positioned within ~50nm from the surface, creating strong field perturbation to the incident wave, whereas the aperture-type THz near-field probes operate at variable distances from the surface. These probes have already been applied for spectroscopic analysis of modes in plasmonic and dielectric sub-wavelength size THz resonators [25,26,29,30]. This study explores the application of aperture-type THz microscopy for direct probing of THz double-metal resonators.

The first resonator type considered here is a classical patch antenna with a high aspect ratio. Our experimental investigations, supported by numerical modelling, reveal two types of fundamental dipolar sub-surface modes, distributed predominantly either in the spacer or in the substrate. The two modes are characterized by different resonance frequencies, however they show a similar spatial field distribution on the sample surface.

The second resonator type considered here is a three-dimensional meta-atom structure consisting of a split-ring resonator and a sub-surface capacitive metallic patch separated by a dielectric spacer layer. This structure, named a *horse-shoe resonator* (HSR) for its shape, was recently proposed for achieving strong electric field confinement [18]. The high symmetry and the subwavelength size of HSRs makes studying its resonances in far-field measurements challenging, particularly for the fundamental mode, which is expected to be dark [19]. Our near-field studies nevertheless show a clear resonance signature in the spectrum. In addition to the fundamental mode, we also observed a higher order resonance, which bears close similarity with the field configuration in planar split-ring structures [32]. The near-field approach thus reveals the difference between the three-dimensional structure with the highly confined sub-surface fields, and the planar split-ring resonators. This study validates the strength of the aperture-type THz near-field microscopy for probing the interaction of THz waves with photonic systems, which provide highly subwavelength electromagnetic confinement.

## 2. Results and Discussion

### *2.1. Resonator design, fabrication and numerical simulations*

We investigated three THz resonators in this work, optical microscope images of the structures are shown in Fig. 1(a). The first resonator is a 48 μm long and 2 μm wide double-metal patch antenna, with a 2 μm thick $SiO_2$ spacer ($n$=2.0) between the metal parts [see details in Fig. 1(b)]. This structure supports standing wave modes with resonance frequencies determined approximately by the expression $f_K=cK/2ns$, where $s$ is the antenna length, $K$ an integer and $c$ the speed of light [33,34]. The fundamental mode is therefore expected at a frequency $f_1$=1.63 THz. This mode was numerically simulated with COMSOL finite-difference time domain (FDTD) solver, and the corresponding electric field distribution in the spacer is shown in Fig. 1(c): the field maxima are located at the edges of the resonator and a node is in the center. More details on modes supported by this resonator will be provided further. We chose a high aspect ratio for the patch antenna, in order to maximize the field leakage [34].

The two other structures are HSRs according to a design from [18]. Optical microscope images and a three-dimensional schematic diagram are shown in Figs. 1(a) and 1(d) respectively. The HSR consist of two metallic parts: a split ring on the surface and a sub-surface rectangular patch. The metallic parts are separated by a 2 μm thick $SiO_2$ layer, with the ends of the split-ring directly above the patch edges. The fundamental resonance of the

structure can be understood in an inductor-capacitor resonator picture [32]: the regions where the two metallic parts are positioned one above the other play the role of capacitors, which store the resonator electric field, while the loop of the surface ring plays the inductor role. The resonator frequency thus can be varied by changing the size of the capacitors, while keeping the same form of the inductive loop.

For the purpose of this study, the resonators were engineered with the fundamental modes in the 1-2 THz range by changing the width $W$ of the double-metal regions, indicated in Fig. 1(a): the $W$=6 μm structure is expected to resonate at 1.3 THz, while the $W$=10 μm structure at 1.1 THz. In Fig. 1(e), we provide the vertical electric field distribution simulated numerically in the spacer for the $W$=6 μm HSR. The field is indeed strongly localized in the double-metal parts. A very similar mode exists in the $W$=10 μm structure.

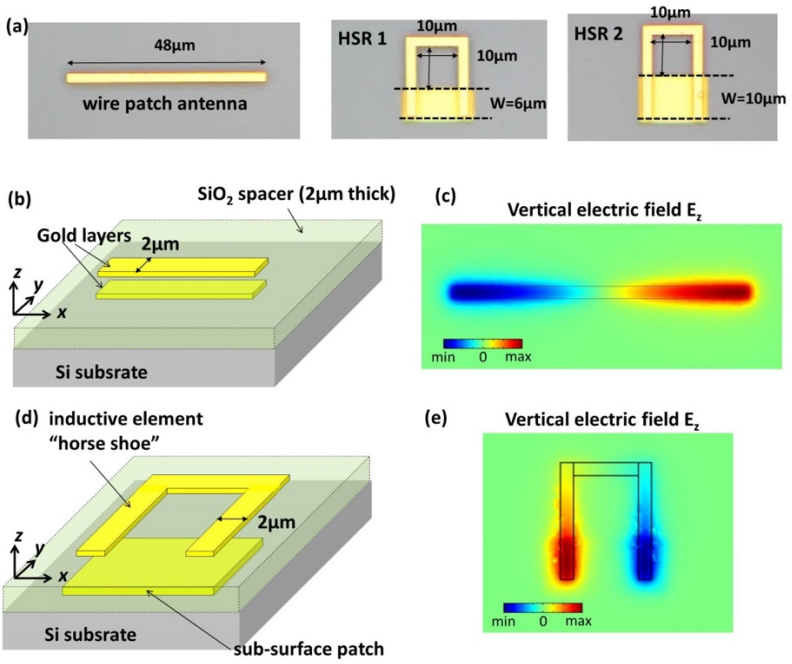


Fig. 1. (a) Optical microscope images of the three types of double-metal resonators studied in this work: wire patch antenna and two HSRs, with relevant dimensions indicated. (b) Schematics of the wire patch antenna, displaying two metal layers and the 2 μm thick $SiO_2$ spacer. (c) Normal electric field $E_z$ for the fundamental resonance of the patch antenna computed at 1.6 THz, in the medium plane of the resonator (COMSOL FDTD simulation). (d) Schematics of the HSR, indicating the top inductive element dubbed "horse shoe" and the sub-surface patch. (e) Normal electric field $E_z$ for the fundamental resonance of the HSR with the 6 μm wide sub-surface plate: the field distribution is computed at 1.3 THz, in the medium plane of the resonator.

All structures were fabricated on the same 300 μm thick Si substrate ($n$=3.4). The lower metallic patch were defined by electron beam lithography (EBL) followed by deposition of 10 nm of Ti and 150 nm of Au. The sample was then covered with a 2 μm thick layer of $SiO_2$ using plasma-enhanced chemical vapor deposition, and the surface metallic loop was defined on top of the $SiO_2$ layer using EBL. The resonators were arranged 150 μm away from each other, in order to avoid interaction between the resonators during experimental THz near-field microscopy and spectroscopy studies.

### *2.2. Near-field THz time-domain spectroscopy of double-metal wire antenna*

To investigate these resonators experimentally, a THz near-field probe was positioned near the resonator as illustrated schematically in Fig. 2(a). We used an aperture-type near-field probe with an embedded THz detector [35]. The top surface of the probe was coated with a 300 nm think layer of gold containing a sub-wavelength size aperture. The THz pulse can couple into the probe only through the aperture, which thus defines spatial resolution of the near-field probe. Two probes with 5 μm and 10 μm apertures were used in these investigations. The embedded THz detector was a photoconductive THz antenna fabricated within 0.5 μm from the aperture plane [35]. The antenna was oriented along the polarization direction of the incident THz beam (*x*-axis). Further details of the experimental system can be found in [29].

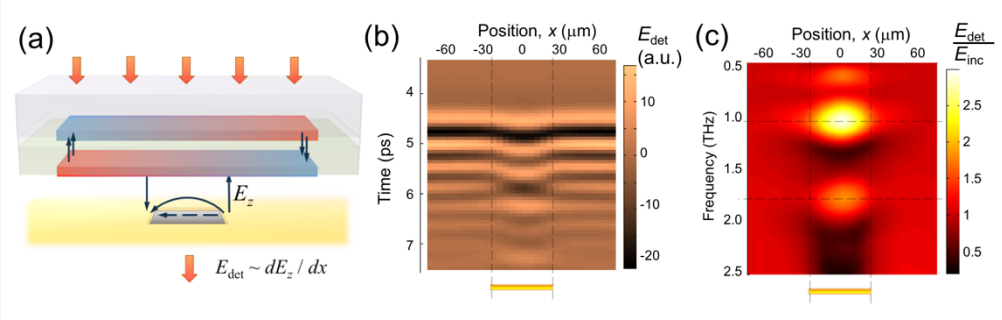


Fig. 2. (a) Schematic diagram of the experiment showing a THz wave incident on the double-metal antenna resonator and a near-field probe with the sub-wavelength input aperture. (b) Space-time map of the field detected along the antenna axis; and (c) the corresponding space-frequency field amplitude map normalized to the incident field spectrum. The map shows two modes at 1.1 THz and 1.8 THz.

The sample was illuminated by short THz pulses (0.5-2.5 THz), which were generated by 100 fs optical pulses in the process of optical rectification in a ZnTe crystal [29]. For the wire patch antenna, we observed an enhanced near-field signal, when the aperture was positioned at the center of the antenna, as shown in Fig. 2(a). We emphasize that although the antenna "blocks" the aperture from the incident THz beam, the coupling of the incident THz wave into the near-field probe nevertheless improves. Enhanced coupling into the aperture can be facilitated by surface waves excited on the antenna surface [23]. The amplitude of the coupled THz field in this case is proportional to the spatial derivative of the $E_z$ component of the surface wave [36].

We scanned the wire antenna in front of the aperture and recorded a space-time map of the detected field [Fig. 2(b)]. The map displays a perturbation in the incident field map within the length of the antenna, similar to the excitation on standing waves on planar antennas [29]. Figure 2(c) shows Fourier transform spectra of the THz field detected along the antenna axis. The spectra are normalized to the amplitude of the incident pulse spectrum. The space-frequency map shows that the field amplitude is enhanced at two frequencies, 1.1 THz and 1.8 THz, and that their spatial distributions are similar, with maxima at the antenna center. The maps in Figs. 2(b) and 2(c) were obtained using the 10 μm aperture probe. We note that a probe with a 5 μm aperture produces identical maps although with lower signal-to-noise ratio.

The detected near-field signal for the double-metal antenna differs from a planar resonator [29]. For the spacer mode, one expects the fundamental resonance with a node of the $E_z$ component in the center of the wire, while the higher order resonances would have multiple nodes and therefore would lead to multiple maxima in the near-field maps. In order to understand the origin of two resonances with similar spatial filed distributions observed in

Fig. 2(c) we preformed COMSOL FDTD simulations of our structure in the range 1-3 THz. The results of these simulations are summarized in Fig. 3. They reveal two fundamental resonances at frequencies of 1.0 THz and 1.6 THz, with identical distributions of the electric field on the surface of the antenna [Figs. 3(a) and 3(c)].

The reason for the difference in resonance frequencies of the two seemingly similar modes is explained in Figs. 3(b) and 3(d): the $E_z$ distribution in the vertical plane ($xz$) is different for the two modes: the 1 THz mode is localized near the interface between the Si substrate and the $SiO_2$ spacer, while the 1.6 THz mode is mainly localized in the $SiO_2$ spacer. This is confirmed by computing the corresponding effective indices according to the formula $f_K=cK/2n_{eff}s$ with $K$=1: we obtain respectively $n_{\text{eff}}$=3.2 for the 1 THz resonance, which is close to the bulk index $n$=3.4 of Si; and $n_{\text{eff}}$=2.03 for the 1.6 THz resonance, very close to the bulk index of $SiO_2$.

More generally, the simulations reveal two families of modes with resonant frequencies consistent with the formula $f_K=cK/2sn_{\text{eff}}$, where $K$ is an integer representing the number of nodes of the electric field $E_z$ along the antenna length [see Figs. 3(a), 3(c), and 3(e)]. Each of the two mode families are described by an effective index $n_{\text{eff}}$. For example, the $K$=1 and $K$=2 modes for $n_{\text{eff}}$~3.4 are illustrated Figs. 3(a) and 3(b), and Figs. 3(e) and 3(f) respectively. Two resonances corresponding to $K$=1 and $K$=2 also exist for $n_{\text{eff}}$ ~ 2 (the $K$=2 resonance at 3.4 THz is not shown).

Interestingly, the simulations results presented in Figs. 3(b), 3(d) and 3(e) show that both the *spacer* modes and the *substrate* modes exhibit some coupling to the top surface via surface waves [23], allowing detection of these modes with the near-field probe. The spatial distribution of the surface waves for both modes is similar to the fundamental dipolar mode distribution on the antenna surface. We therefore conclude that the experimentally observed resonances in Fig. 2(c) correspond to the spacer and substrate modes of the double-metal resonator; and that these modes couple to the air region via the surface wave mechanism, and thus can be detected by the aperture-type near-field probe. The numerical values of the resonant frequencies (1.0 and 1.6 THz) are close to the measured values of 1.1 THz and 1.8 THz. The difference will be explained in the following section.

The spectral peaks in the experiment displayed different amplitudes: the low-frequency substrate peak was higher compared to the spacer peak. Two factors can affect the observed resonance strength: the coupling efficiency and the probe sensitivity at different frequencies. To identify the main factor in our experiment, we performed numerical simulations of the antenna structure together with the aperture probe positioned above the antenna, at a distance of $h$=5 μm from the surface. We found that for the same excitation intensity at two frequencies, the substrate mode induces a stronger field in the aperture compared to the spacer mode, with the field amplitude 2.75 times higher. Since the near-field probe is more sensitive at higher frequencies, due to the aperture transmission dependence [37], the higher amplitude for the lower frequency peak indicates that its coupling efficiency is higher for the substrate compared to the spacer mode.

This finding is in agreement with the experimental observations (Fig. 2), where the 1.1 THz peak (corresponding to the substrate mode) was detected with amplitude of almost 2 times higher compared to the 1.8 THz peak (spacer mode). The spectrum in Fig. 2(c) was normalized to the spectrum of the incident pulse detected by the near-field probe. The normalization was applied to compensate for the difference in amplitudes of spectral components in the incident pulse, and for the frequency dependent sensitivity of the near-field probe.

The relatively inefficient excitation of the spacer mode can be understood intuitively when considering excitation of the upper and the lower antenna separately. We note that the thickness $T$ of the spacer separating the antennas was small compared to the resonant wavelength λ ($T/\lambda$ ~0.01). Therefore any propagation effects can be neglected, and the two antennas are excited almost in phase. The spacer mode however requires charges oscillating

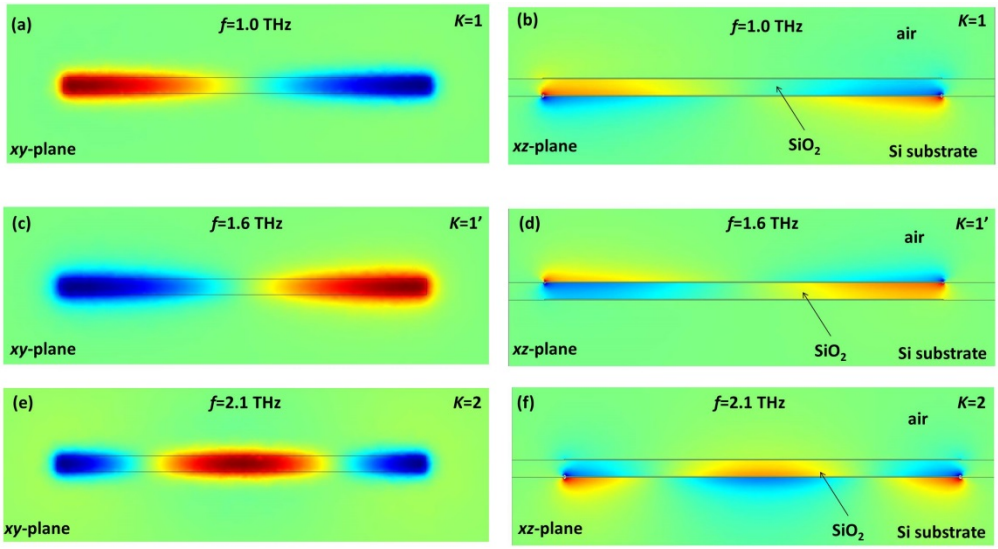


Fig. 3. FDTD simulations of the electric field component $E_z$ for the first three resonant modes of the wire patch antenna resonator: (a) distribution of $E_z$ in the *xy*-plane in the middle of the spacer layer for the fundamental $K$=1 resonance at $f$=1.0 THz; (b) distribution of $E_z$ in the *xz*-plane along the antenna length for the $K$=1 resonance at $f$=1.0 THz; (c, d) maps of of $E_z$ in the *xy* and *xz* planes respectively for the $K'$=1 resonance at f=1.6 THz; (e, f) maps of $E_z$ in the *xy* and *xz* planes respectively for the $K$=2 resonance at $f$=2.1 THz.

on the two antennas with a phase difference of $\pi$. Therefore coupling to the spacer mode for the free-space waves is not efficient. Our experimental and numerical results confirm that the incident field couples better to the substrate mode compared to the spacer mode for the dipole antenna geometry. In general however, the coupling efficiency may depend on a number of factors, such as the refractive indices of the substrate and spacer, and the spacer thickness.

### *2.3. Near-field probe interaction with antenna resonator: Image interpretation and Near-field effect on resonance frequency*

In this section, we describe our numerical modelling of the signal detected by the near-field probe, and the effect of the probe on the antenna resonant frequency. The experimental 2D space-frequency map in Fig. 2(c) shows that the spatial distribution of the detected field for both resonances is different from the 2D maps of the electric field on the resonator surface obtained numerically [Figs. 3(a) and 3(c)]. Indeed, the amplitude of the electric field on the surface is maximal at the patch antenna edges, whereas the maximum signal was detected near the antenna center [Fig. 2(c)].

To explain this behavior we performed COMSOL FDTD simulations of the entire probe+antenna system, as shown in the simulation layout in Fig. 4. The signal detected by the probe was estimated from the horizontal electric field distribution ($E_x$) within the probe aperture. This component of field defines the potential difference that appears between the edges of the probe aperture, $DV = -\int_{\substack{probe \\ aperture}} E_x dx$, which is proportional to the current induced in the probe [23,36]. The metallic screen of the probe was modelled as a perfect conductor, while the metal of the antenna was modelled with a refractive index $n$=300+$i$*500, which was estimated from measurements of the skin depth using the Drude model [38]. The distance between the antenna surface and the probe $h$ was varied in order to evaluate the effect of the probe on the antenna resonance.

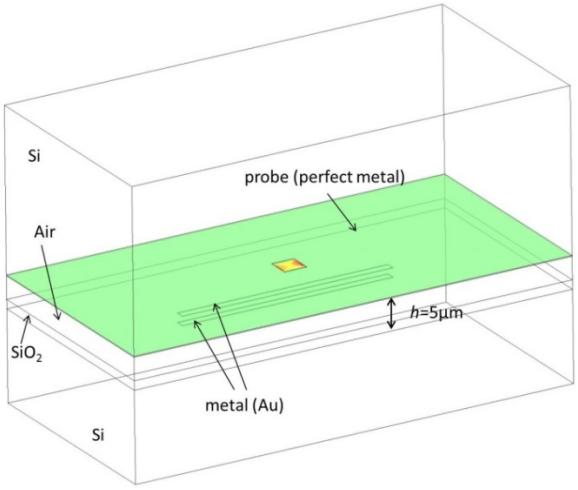


Fig. 4. Layout for 3D modelling of the near-field detection of the resonator field by the subwavelength aperture probe. The probe surface is modelled as a perfect metallic plane with an aperture, whereas the double-metal antenna is modelled as a real metal with an imaginary index $n$=300+$i$*500, according to values form [38]. The electric field component $E_x$ is plotted in the plane of the screen. The distance between the probe and the antenna $h$ = 5 μm.

We simulated the field distribution within the aperture for two principal positions of the probe: at the antenna center and at the antenna edge, with the distance between the antenna and the probe $h$=5 μm. The field maps are shown in Figs. 5(a) and 5(c). They illustrate different distributions of the field within the aperture: for the aperture position above the antenna center, the electric field induced within the aperture is of one direction, whereas the field distribution for the aperture positioned at the antenna edge is symmetric with respect to the aperture center.

Figures 5(b) and 5(d) schematically illustrate the corresponding electric field lines connecting the patch antenna and the probe for each case. Let us recall that the patch antenna resonance has a quadrupole charge distribution, as shown in Figs. 5(b) and 5(d). Indeed, the surface charge density σ induced on the metal walls can be inferred directly from the vertical electric field component $E_z$ according to Gauss law $\sigma=\varepsilon_0 E_z$. When the aperture is positioned at the antenna center [Fig. 5(a)], there are charges of opposite signs induced on the opposing edges of the probe aperture; and the field lines start from the positive charges and terminate at the negative ones. The integral value of the potential difference ($DV$) is thus non-zero.

On the contrary, a polarized antenna induces charges of the same polarity at the opposite edges of the aperture when the probe is placed at the antenna edge. As a result, we expect that the field integrated over the aperture surface, and thus the potential difference ($DV$) between the aperture edges vanishes when the aperture is positioned at the antenna edges, and no signal is detected by the near-field probe.

Charge conservation dictates that negative charges must accumulate at the other edges of the probe aperture, as shown in Fig. 5(c). This was confirmed numerically by the $E_y$ component distribution in the probe aperture, which is very similar to the results for $E_x$, only rotated by 90°. The $E_y$ field however does not contribute to the potential difference integral and therefore does not contribute to the detected signal.

More generally, this analysis clarifies that the signal detected by the probe is proportional to the derivative of the surface charge density $d\sigma/dx$, and thus proportional to $dE_z/dx$ as indicated in Fig. 2(a) [34]. The near-field signal generated in the probe can thus be explained by electrostatic arguments, while somehow similar reasoning (this time applied to the symmetry of the charge distribution of the antenna) explains the far-field coupling [19].

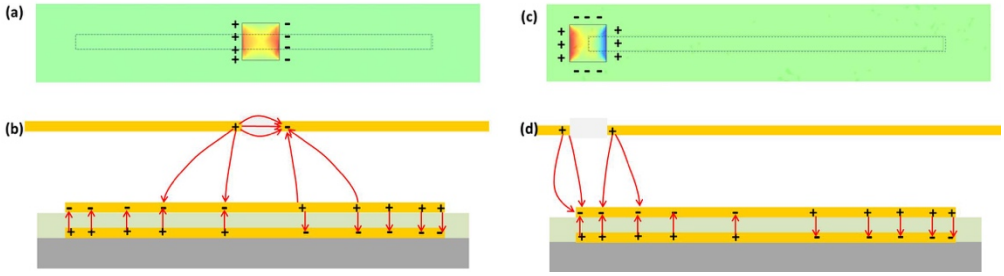


Fig. 5. (a) Electric field map of the in-plane component $E_x$ of the electric field on the surface of the probe for the case of the aperture positioned above the center of the antenna [see Fig. 1(b) for definition of the coordinate system]. (b) Sketch of the electric field lines in the $xz$-plane. (c) Electric field map of $E_x$ for the case of the probe positioned above the antenna edge, and (d) the corresponding sketch of electric field lines.

We note that the experimentally measured spatial profile of the detected signal is similar to the magnetic field distribution near a planar antenna [39]. Aperture-type near-field probes were shown to produce images of the magnetic field distribution [39,40]. However, the numerical simulations presented above show that in our case, the detected signal is related to the electric field induced in the aperture by the surface charge density in the polarized antenna.

The resonant fields therefore can be experimentally detected and analyzed with the aperture of the near-field probe positioned above the center of the antenna. We recorded waveforms of the detected field for different distances between the near-field probe and the sample surface $h$. The waveforms and the corresponding normalized Fourier spectra are shown as field maps in Figs. 6(a) and 6(b) respectively.

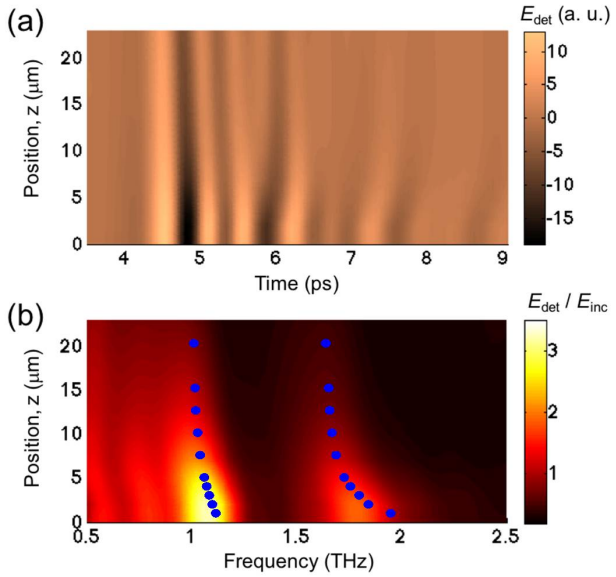


Fig. 6. (a) Space-time ($zt$) map of the field detected at the antenna center for different values of the spacing $h$ between the probe and the resonator; (b) corresponding normalized space-frequency map showing two modes. The blue dots correspond to the resonant frequencies found in the COMSOL FDTD simulations.

The sample-probe distance $h$ affects both the strength of the detected field and its temporal evolution. The Fourier map in Fig. 6(b) allows us to interpret the changes: both the spacer and the substrate modes experience resonance frequency shifts toward lower frequencies and decrease in amplitude as $h$ increases. The shifts are pronounced for smaller gaps, $h$<5 μm. For gaps $h$>10 μm however, the resonance frequency remains practically unchanged. The two resonances can be still detected at $h$=20 μm.

To identify mechanisms responsible for the effect of the probe on the resonator modes, we numerically modelled resonance frequencies in the presence of the probe using FDD simulations as described above. We computed the eigenmodes of the whole antenna+probe system with a variable spacing $h$. The results, indicated by dots in Fig. 6(b), reproduce the experimentally observed frequency shift. As in the experiment, the probe has little influence on the antenna modes for $h$>5 μm, and the simulated spectrum approaches the "bare" antenna spectrum found in previous simulations with resonances at 1.0 THz and 1.63 THz.

The simulations indicate that the sharp increase of the measured frequencies for $h$<5μm is due to field concentration in the air gap between the probe and the antenna. As air has the lowest refractive index $n$=1, the modal effective index $n_{\text{eff}}$ decreases producing a blueshift of the resonant frequency according to the expression $f_{\text{res}}=c/2n_{\text{eff}}s$. The substrate mode, which is distributed deep underneath the surface, is affected by the near-field probe to a smaller degree compared to the spacer mode, which experiences a larger frequency shift, from 1.6 THz to >1.9 THz. This frequency shift caused by the interaction with the near-field probe can be exploited for 'tuning' the resonance frequency in investigations of light-matter coupling. The near-field probe in this case could act both as a detector and the tuning element.

### *2.4. Near-field spectroscopy and imaging of horseshoe resonators*

In this section we discuss our investigations of HSRs shown in Figs. 1(a), 1(d) and 1(e). Experimental near-field characterization was performed similarly to the antenna characterization. Figure 7(a) shows an example of the instantaneous field distribution detected by the near-field probe with a 10 μm aperture. The subsurface metal patch appeared as a bright area in the image. The outline of the upper loop was also visible, despite the large size of the aperture compared to the loop, which was 2 μm in width. We note that as in the case of the antenna sample, the near-field probe detected sample features narrower than the aperture size. We attribute this to the surface wave nature of the detected fields.

To characterize the spectral signature of the HSRs, space-time maps were measured along two line scans, parallel and perpendicular to the sub-surface patches. Figures 7(b) and 7(c) show normalized Fourier spectra of the detected field. For the first design, HSR1, we observed field enhancement in the area of the patch at two frequency bands: at ~1.65 THz, and at ~2.4 THz. We note that the second band was near the upper limit of the detector sensitivity range, and thus we could not determine the central frequency of this band accurately. We also observed some field enhancement at 1.2 THz, however the line scans showed that this field was not localized at the resonator and therefore it is not attributed to the resonator modes and won't be discussed here. For the second design, HSR2, the field enhancement spectrum also showed two modes, at lower frequencies (1.4 and 2.4 THz) as expected for a larger size resonator.

As discussed in Section 2.1, resonant frequencies for the fundamental modes in HSR1 and HSR2 were numerically found to be 1.3 THz and 1.1 THz, whereas in the experiment, we found resonant field enhancement at 1.65 THz and 1.4 THz respectively. We note that the numerical results in Sec. 2.1 were calculated for the bare resonators, without taking into account the near-field probe that interacts with the resonators in the experiment. The probe tends to shift some of the resonator energy from the high index substrate into the air gap between the probe and the antenna. Due to the low refractive index of air, the effective index

therefore decreases producing a blue shift in the resonant frequency similarly to the effect observed in the antenna resonator (Sec. 2.3, Fig. 6).

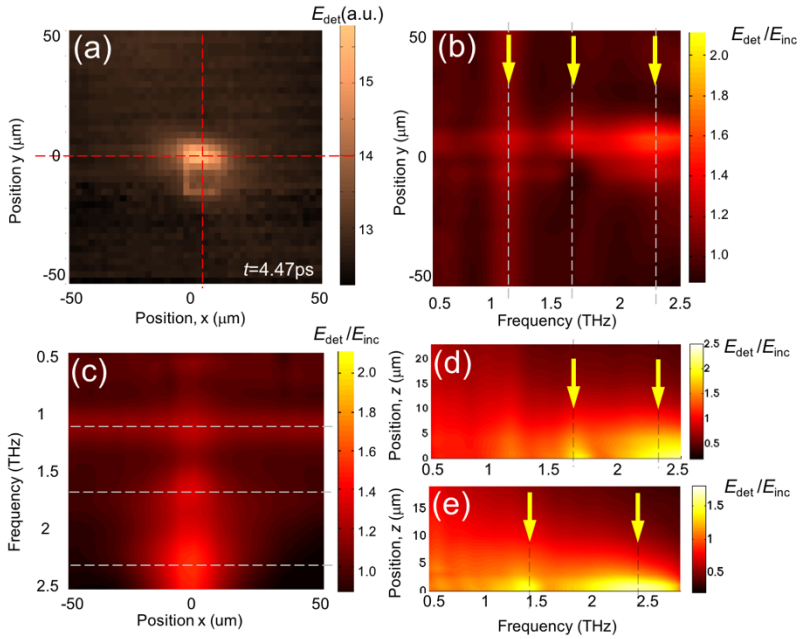


Fig. 7. (a) Instantaneous field distribution (*xy*) detected near the horseshoe resonator surface (image size: 100 μm × 100 μm); (b,c) space-frequency maps (*yt* and *xt* respectively) of the normalized field amplitude detected along line scans indicated by the dashed lines in (a); (d,e) normalized space-frequency maps of the detected field for different positions (*z*) of the aperture above the resonator surface.

To gain insight into the nature of the excited resonances, we performed numerical simulations with CST Microwave Studio of the HSR1 structure together with the near-field probe, excited by a THz pulse incident normally from the side of the Si substrate, as in the experiment. The optical refractive indexes of different layers and the structure geometry were identical to the ones used with COMSOL simulations. The near-field probe was positioned at a distance of $h$=5 μm away from the resonator. To model the experimentally detected signal, we calculated the amplitude of the electric field $E_x$ at the center of the probe aperture. The field amplitude normalized to the amplitude of the incident wave is shown in Fig. 8(a) as a function of frequency. The simulation results are in close agreement with the experiment for the HSR1 [Fig. 7(d)]: the spectrum displays two resonant features at 1.6 THz and 2.55 THz, with a well pronounced minimum between the two.

We further analyzed the field distribution for each of the maxima observed in the spectrum. Figure 8(b) shows the distribution of the normal field $E_z$ for the first mode, which also corresponds to the fundamental mode of the HSR described in Fig. 1(e). In that case, the electric field is strongly concentrated between the two metal regions [see the *side view* in Fig. 8(b)]. The field distribution of the second resonant feature around 2.55 THz is illustrated in Fig. 8(c). Now the field is distributed along the entire length of the HSR arms [*top view*], similar to the fundamental mode of a planar split-ring resonator of this shape [32].

According to our analysis of wave coupling into the probe aperture, we expect that the fundamental mode of the resonator produces maximum near-field signal when the aperture is positioned above the sub-surface patch, where the aperture faces charges of opposite signs and $dE_z/dx$ is maximized. The bright spot in the map in Fig. 7(b) is thus consistent with the fundamental mode.

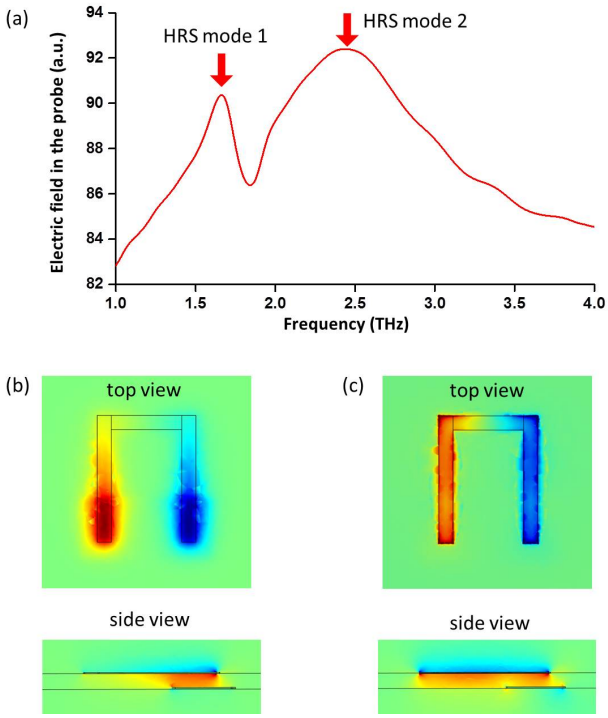


Fig. 8. (a) COMSOL FDTD simulations of electric field coupled into the probe as a function of frequency. The electric field amplitude was normalized to the amplitude of the incident wave. (b) Electric field $E_z$ maps for Mode 1 in the HSR (1.6 THz), excited with the polarization field vector along the *x*-axis. The *top view* panel shows the field distribution in the *xy*-plane in the spacer layer, and the *side view* shows the field distribution in the *yz*-plane crossing the HSR arm. (c) Electric field $E_z$ maps for Mode 2 at 2.55 THz.

We note that this fundamental mode bears a high symmetry and it is a dark mode, which was undetectable in far-field experiments [19]. The field distribution for the second mode is rather dipolar, and therefore this mode is expected to couple better to the incident wave compared to the fundamental mode. The second mode is delocalized and the field is lumped around the surface of the top loop, only weakly interacting with the bottom patch [*side view* in Fig. 8(c)]. The delocalization is consistent with the experimental map in Fig. 7(b), where the 2.5 THz peak is distributed along the *y*-axis, in contrast to the 1.6 THz peak, which is localized at the sub-surface patch area.

The split-ring mode signature has a broader character compared to the spacer mode. We attribute this to a higher radiation loss, which is expected for the dipolar distribution shown in Fig. 8(c). There is a pronounced minimum between the two spectral peaks, which is reminiscent of a Fano-like coupling between a sub-radiant mode (HSR mode 1) and a super-radiant mode (HSR mode 2), as observed in a variety of systems [41-43]. We thus conclude that the minimum between the two peaks in Fig. 8(a) corresponds to destructive interference of the two spectrally-overlapping coherently excited modes.

There is a good agreement between the numerical simulations and the experimental data. We thus conclude that the near-field probe positioned directly above the sub-surface patch enables detection of two resonator modes, including the fundamental mode with strong field confinement in the space layer. We note that due to the deep subwavelength size of the HSR, the resonant fields were detected only within ~10 μm from the surface, and the effect of the probe on the resonance frequency was not as significant as in the case of the antenna.

## 3. Conclusions

We investigated the use of aperture-type THz near-field microscopy for local spectroscopy of double-metal THz resonators in two geometries: the classical double-metal patch antenna with a 2 μm spacer layer and the recently proposed subwavelength-size three-dimensional meta-atom resonator [18,19]. Despite the strong mode confinement of the double-metal design, the near-field probe enables local THz spectroscopy of the excited modes.

Surface waves play a key role in enabling detection of the strongly-localized modes in double-metal resonators. A fraction of the mode energy couples to the resonator surface and thus can be detected by a near-field probe. The aperture-type photoconductive THz near-field probes, employed here, enable local spectroscopic analysis of individual double-metal THz resonators, revealing modes, which exhibit poor coupling to propagating waves.

For the antenna geometry, we observed two modes with similar spatial distribution on the surface of the resonator. Our numerical analysis identified these modes as the fundamental dipolar modes distributed either in the dielectric spacer region or in the high-index substrate. The simulations also supported the mechanism for near-field detection of these highly confined modes. The metallic surface of the near-field probe was found to impact the resonance frequency, when the probe is positioned at distances below 5 μm away from the resonator. The presence of the metallic surface leads to an increase of the resonance frequency above the frequency of the bare resonator. This dependence can be used for tuning the resonance frequency by ~15%, and thus the technique can enable investigations of polariton coupling [44].

The near-field probe also enabled THz spectroscopy of single resonators, which exhibit THz field localization to a higher degree comparted to the patch antenna. Two spectrally overlapping THz modes were detected in the HSR with the footprint of 14x18 $\mu m^2$. The lower frequency mode (1.6 THz) is a dark mode, which was not detected in far-field experiments previously [19]. The spectral overlap of the two HSR modes leads to local interference of the resonant fields and a Fano-like shape of the near-field spectrum.


### Funding

The Royal Society (UF130493), ERC ("ADEQUATE"), French National Research Agency (ANR-16-CE24-0020 Project "hoUDINi"), and the EPSRC (EP/P021859/1).

### Acknowledgments

Fabrication of THz near-field probes was performed, in part, at the Center for Integrated Nanotechnologies, an Office of Science User Facility operated for the U.S. Department of Energy (DOE) Office of Science. Sandia National Laboratories is a multi-program laboratory managed and operated by Sandia Corporation, a wholly owned subsidiary of Lockheed Martin Corporation, for the U.S. Department of Energy's National Nuclear Security Administration under Contract No. DE-AC04-94AL85000.